*Article*

# The Potential of Time Series Merged from Landsat-5 TM and HJ-1 CCD for Crop Classification: A Case Study for Bole and Manas Counties in Xinjiang, China

**Pengyu Hao [1,2], Li Wang [1,]\*, Zheng Niu [1], Abdullah Aablikim [3], Ni Huang [1], Shiguang Xu [1] and Fang Chen [4]**

[1]  The State Key Laboratory of Remote Sensing Science, Institute of Remote Sensing and Digital Earth, Chinese Academy of Sciences, Beijing 100101, China; E-Mails: haopy@radi.ac.cn (P.H.); niuzheng@radi.ac.cn (Z.N.); huangni@radi.ac.cn (N.H.); xusg@radi.ac.cn (S.X.)

[2]  University of Chinese Academy of Sciences, Beijing 100049, China

[3]  Xinjiang Survey Organization, National Bureau of Statistic of China, Xinjiang 830001, China; E-Mail: aablikim@163.com

[4]  Key Laboratory of Digital Earth Science, Institute of Remote Sensing and Digital Earth, Chinese Academy of Sciences, Beijing 100094, China; E-Mail: fangchen@ceode.ac.cn

**\***  Author to whom correspondence should be addressed; E-Mail: wangli@radi.ac.cn; Tel.: +86-10-6480-6252.

**Abstract:** Time series data capture crop growth dynamics and are some of the most effective data sources for crop mapping. However, a drawback of precise crop classification at medium resolution (30 m) using multi-temporal data is that some images at crucial time periods are absent from a single sensor. In this research, a medium-resolution, 15-day time series was obtained by merging Landsat-5 TM and HJ-1 CCD data (with similar radiometric performances in multi-spectral bands). Subsequently, optimal temporal windows for accurate crop mapping were evaluated using an extension of the Jeffries–Matusita (JM) distance from the merged time series. A support vector machine (SVM) was then used to compare the classification accuracy of the optimal temporal windows and the entire time series. In addition, different training sample sizes (10% to 90% of the entire training sample in 10% increments; five repetitions for each sample size) were used to investigate the stability of optimal temporal windows. The results showed that time series in optimal temporal windows can achieve high classification accuracies. The optimal temporal windows were robust when the training sample size was sufficiently large. However, they

were not stable when the sample size was too small (*i.e.*, less than 300) and may shift in different agro-ecosystems, because of different classes. In addition, merged time series had higher temporal resolution and were more likely to comprise the optimal temporal periods than time series from single-sensor data. Therefore, the use of merged time series increased the possibility of precise crop classification.

## 1. Introduction

Multi-temporal remote sensing data can be used to describe changes in vegetation characteristics over time [1–3], and cropland distribution maps can be produced by classifying multi-temporal remote sensing images throughout the growing season [4–6]. At medium spatial resolution (10–100 m), multi-temporal Landsat-5 Thematic Mapper (TM) images, with 30-m spatial resolution and a 16-day revisit frequency, have a proven potential for crop classification [7,8]. Although images of key time-periods are sufficient for accurate crop mapping [9–11], misclassification may still occur, because cloud-free images that cover all critical periods are difficult to obtain from large areas using a single sensor, such as the Landsat-5 TM.

The Huan Jing Constellation satellite system, launched in 2008, was expected to overcome these limitations, because HJ-1 CCD data have high temporal resolution (four days) and similar wavebands (near-infrared, red, green and blue), medium spatial resolution (30 m) and radiometric calibration performance to Landsat-5 TM [12]. Previous research has demonstrated the potential of HJ-1 CCD data for distinguishing crop types [11,13]. However, there are only a few studies in which Landsat 5 TM data were merged with HJ-1CCD data to obtain a dense time series at 30-m spatial resolution for crop mapping.

Therefore, the objectives of this research are as follows: (1) to compare the radiometric performance of Landsat-5 TM and HJ-1 CCD data; (2) to select the optimal temporal windows for accurate crop classification from a time series obtained by merging Landsat-5 and HJ-1 CCD data; (3) to evaluate the potential of time series data for an entire growing season and from optimal temporal windows for crop mapping using a support vector machine (SVM); and (4) to detect the stability of optimal temporal windows when different training sample sets are used. We employed both multi-spectral bands and NDVI in this research, because spectral diversity provides a richer source of information for accurate crop classification [14].

## 2. Study Regions and Datasets

### 2.1. Description of Study Area and Crop Calendar

For this study, we selected two representative agricultural regions in northern Xinjiang. One is located in Bole County, which contains 32 kha of cropland (44°20′–45°23′N, 80°40′–82°42′E), and the other is located in Manas County, which has 180 kha of cropland (43°17′–45°20′N, 85°17′–86°46′E)

(Figure 1a–c). Both regions have a temperate continental climate that is characterized by dry weather and drought. The annual average temperature and rainfall are 7.0 °C and 202.4 mm in Bole and 7.2 °C and 208.2 mm in Manas, respectively.

**Figure 1.** Study areas. (**a**) Location of Bole and Manas Counties in Xinjiang. (**b**) Bole (11 July 2011); and (**c**) Manas (13 July 2011). The images are standard false color composites of Landsat-5 TM. The green patterns on the images show the distribution of ground-truth data. (**d**) Vegetation cover fractions for different crop types over the course of a year.
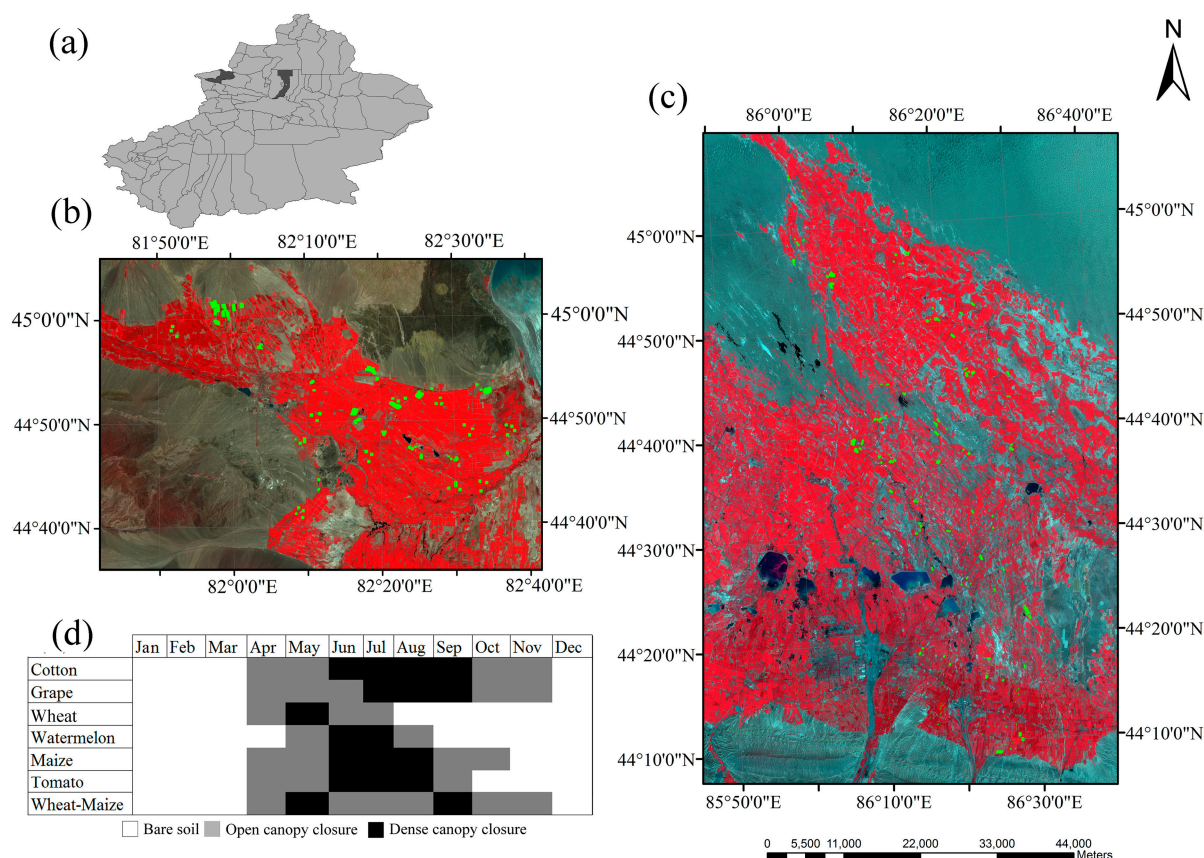


The dominant crops grown in the study areas include cotton, maize, watermelon, grape, tomato, wheat-maize and wheat. The vegetation cover fraction for each crop type over the course of a year is presented in Figure 1d; black boxes represent a dense canopy closure; grey boxes represent open canopy closure; and white boxes represent bare soil or, from November until March, snow. The planting dates for cotton, maize, watermelon, tomato and grape are in early April, while wheat is mostly planted in early November to begin growth in April. In addition, summer maize is planted as a second crop during early August (after the planting period of wheat). Cotton, grape, maize and watermelon grow mostly during the June–July period, while wheat grows mostly during April. The harvest date for wheat is in late June, while, among the summer crops, watermelon and tomato are harvested in August, maize is harvested in early September and grapes and cotton are harvested during the August–September and September–October periods.

## 2.2. Datasets

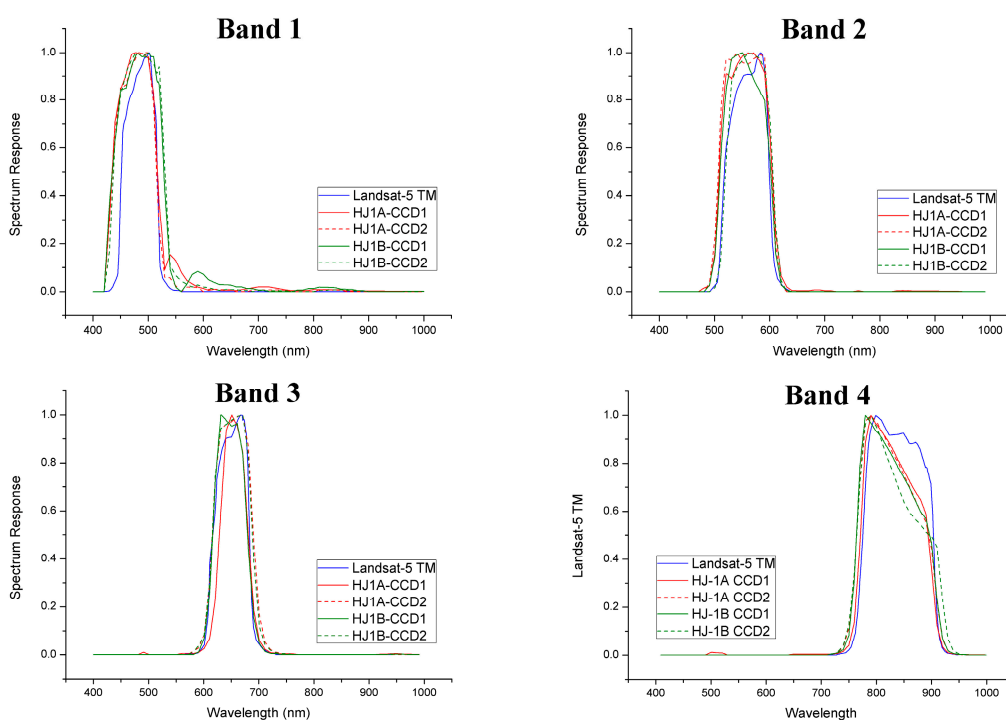### 2.2.1. Landsat-5 TM and HJ-1 CCD Data

The Huan Jing (HJ) Constellation satellites were launched by the Chinese government in 2008. HJ-1 has two satellites (HJ-1A and HJ-1B), and each satellite has two CCD cameras. The HJ Constellation has a 720-km lateral coverage, 30-m spatial resolution, which is similar to TM images, and a temporal resolution of four days. The CCD cameras have three visible bands and one near-infrared band. Table 1 and Figure 2 show the similarity in spectral response function and spectral bands of Landsat-5 TM and HJ-1 CCD [15,16]. Landsat-5 has a revisit time of 16 days, but cannot cover an entire growing season at its 15-day temporal resolution, because of cloud cover. Therefore, we merged Landsat-5 TM and HJ-1 CCD images to obtain an image time series at a 15-day temporal resolution.

**Table 1.** Landsat-5 TM and HJ-1 CCD spectral bands.

| | Landsat-5 TM Spectral Bands | | | HJ-1 CCD Spectral Bands | |
|---|---|---|---|---|---|
| # | Band Width (μm) | GSD (m) | # | Band Width (μm) | GSD (m) |
| 1 | 0.45–0.515 | 30 | 1 | 0.43–0.52 | 30 |
| 2 | 0.525–0.605 | 30 | 2 | 0.52–0.60 | 30 |
| 3 | 0.630–0.690 | 30 | 3 | 0.63–0.69 | 30 |
| 4 | 0.775–0.900 | 30 | 4 | 0.76–0.90 | 30 |
| 5 | 1.550–1.750 | 30 | | | |
| 7 | 2.090–2.350 | 30 | | | |

GSD: ground sample distances.

**Figure 2.** The spectrum response function of multi-spectral bands of the Landsat-5 TM and HJ1A/B CCD.

The images used in this study are listed in Table 2. First, data from both sensors (Landsat-5 TM and HJ-1 CCD) were obtained (Numbers 12–14 and the TM images in bold in Table 2) to estimate the similarity between Landsat-5 TM and HJ-1 CCD images during three different time periods. Then, all images with a cloud cover of less than 10% (Numbers 1–11 in Table 2) were used to acquire the time series with an approximate 15-day temporal resolution. The Landsat-5 TM reflectance product (CDR) [17] and the HJ Level 2 product were used in this study.

**Table 2.** Landsat-5 TM and HJ-1 CCD images for both study regions.

| Number | Bole | | Manas | |
|---|---|---|---|---|
| | **Data** | **Sensor Name** | **Data** | **Sensor Name** |
| 1 | 6 April 2011 | TM | 24 April 2011 | TM |
| 2 | 22 April 2011 | TM | **10 May 2011** | **TM** |
| 3 | 10 May 2011 | HJ1B-CCD1 | 28 May 2011 | HJ1B-CCD2 |
| 4 | **24 May 2011** | **TM** | 28 June 2011 | TM |
| 5 | 8 June 2011 | HJ1A-CCD1 | **13 July 2011** | **TM** |
| 6 | 11 July 2011 | TM | 29 July 2011 | TM |
| 7 | **27 July 2011** | **TM** | 15 August 2011 | HJ1B-CCD2 |
| 8 | 16 August 2011 | HJ1B-CCD1 | 16 September 2011 | HJ1B-CCD1 |
| 9 | **13 September 2011** | **TM** | **1 October 2011** | **TM** |
| 10 | 27 September 2011 | HJ1A-CCD1 | 15 October 2011 | HJ1A-CCD2 |
| 11 | 16 October 2011 | HJ1A-CCD2 | 27 October 2011 | HJ1A-CCD2 |
| 12 | 23 May 2011 | HJ1A-CCD2 | 10 May 2011 | HJ1A-CCD2 |
| 13 | 29 July 2011 | HJ1A-CCD2 | 13 July 2011 | HJ1A-CCD1 |
| 14 | 14 September 2011 | HJ1A-CCD2 | 1 October 2011 | HJ1B-CCD2 |

Images were georeferenced to the UTM WGS 84 zones, 44N (Bole) and 45N (Manas). The HJ images were registered to the TM images, achieving an RMSE of less than 0.3 pixels using a second order polynomial transformation and bi-linear resampling. Subsequently, radiance calibration and FLAASH atmospheric correction were performed using ENVI for HJ-1 CCD images [18]. Together with the reflectance of multi-spectral bands, the Normalized Difference Vegetation Index (NDVI) was used in this research, because NDVI can describe the phenological characteristics of different crops. We used visible (red) and near-infrared (NIR) bands to calculate NDVI (Equation (1)).

$$NDVI = \frac{\rho(NIR) - \rho(Red)}{\rho(NIR) + \rho(Red)} \tag{1}$$

where $\rho(NIR)$ and $\rho(Red)$ are the reflectance values of the NIR and red bands, respectively.

2.2.2. Ground-Truth Data

Ground-truth data were obtained by fieldwork in the study regions during 2011. Fields were selected to represent the full variety of crop types and an even distribution across the study areas. A total of 525 fields in Bole and 459 fields in Manas were selected and surveyed. For each field, the crop type was collected as attribute information. Field boundaries were recorded using GPS and digitized as polygons in ArcGIS. To avoid boundary pixels, polygons were converted to a raster format using the TM grid. In total, 9,084 sample pixels for Bole and 8490 pixels for Manas were obtained.

The distribution of ground-truth data is shown in Figure 1. The amounts of training and validation samples for each crop type are shown in Table 3.

**Table 3.** Number of surveyed fields, training samples and validation samples.

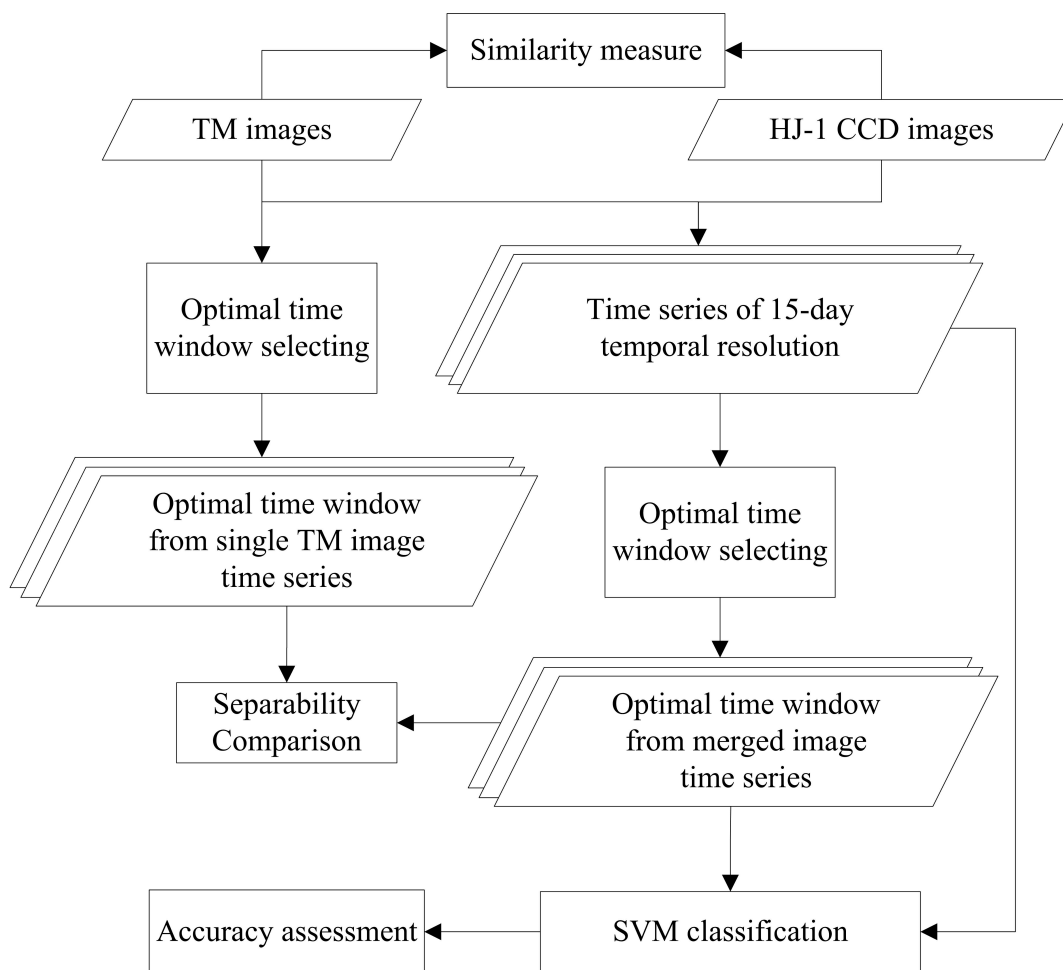| Crop Types | Bole | | | Manas | | |
|---|---|---|---|---|---|---|
| | **Surveyed Fields** | **Training** | **Validation** | **Surveyed Fields** | **Training** | **Validation** |
| Cotton | 229 | 500 | 4542 | 269 | 350 | 4081 |
| Maize | 36 | 150 | 477 | 63 | 300 | 1674 |
| Grape | 43 | 300 | 1143 | 0 | 0 | 0 |
| Wheat | 74 | 350 | 1038 | 54 | 300 | 1468 |
| Wheat-Maize | 68 | 200 | 840 | 28 | 50 | 434 |
| Watermelon | 75 | 350 | 1044 | 0 | 0 | 0 |
| Tomato | 0 | 0 | 0 | 45 | 150 | 833 |
| Total | 525 | 1850 | 9084 | 459 | 1150 | 8490 |

## 3. Methods

The overall methodology used in this study is presented in Figure 3. First, we evaluated the similarity between Landsat-5 TM and HJ-1 CCD images by comparing the NDVI and land-surface reflectance of multi-spectral bands. Then, Landsat-5 TM and HJ-1 CCD images were merged to build a time series with a 30-m spatial and 15-day temporal resolution. Multi-spectral bands and NDVI time series of the training and validation pixels were extracted, and further analysis was based on the extracted multi-spectral and NDVI time series. Afterwards, the most relevant time windows were selected from both merged and single TM time series using an extension of the Jeffries–Matusita (JM) distance. Then, a comparison between utilizing optimal temporal windows and the entire merged time series for classification was conducted by analyzing overall accuracies, and a support vector machine (SVM) was selected as the classifier. In addition, the stability of the optimal temporal windows relative to the training sample size was determined for both study regions. The size of the sample sets varied from 10% to 90% of the entire training sample size in 10% increments. Five random repetitions were selected for each sample size.

### 3.1. Similarity Evaluation between Landsat-5 TM and HJ-1 CCD Data

We evaluated the radiometric similarity between Landsat-5 TM and HJ-1 CCD data by comparing the land-surface reflectance and NDVI of the two sensors for similar dates. To reduce the potential impacts of registration inaccuracy (Section 2.2), we defined subsets of homogeneous regions of interest (ROI) with $3 \times 3$ windows located in the middle of larger homogeneous "patches" [12]. Average values of these sampling windows were used to compare similarities between Landsat-5 TM and HJ-1 CCD images. Through this process, we defined subsets of the ROIs for different crop types, selecting 170 and 153 windows within Bole and Manas, respectively. Scatter plots and linear relationships were used to examine how Landsat-5 TM and HJ-1 CCD images differed in performance.

**Figure 3.** Methodology used in this study.

```
                    ┌──────────────────────┐
          ┌────────►│  Similarity measure  │◄────────┐
          │         └──────────────────────┘         │
   ┌──────┴──────┐                          ┌─────────┴────────┐
   │  TM images  │                          │  HJ-1 CCD images │
   └──────┬──────┘                          └─────────┬────────┘
          │                                           │
          ▼                                           ▼
┌──────────────────┐                        ┌──────────────────┐
│   Optimal time   │                        │ Time series of   │
│ window selecting │                        │ 15-day temporal  │
└────────┬─────────┘                        │   resolution     │
         │                                  └────────┬─────────┘
         ▼                                           ▼
┌──────────────────┐                        ┌──────────────────┐
│ Optimal time     │                        │   Optimal time   │
│ window from      │                        │ window selecting │
│ single TM image  │                        └────────┬─────────┘
│ time series      │                                 │
└────────┬─────────┘                                 ▼
         │                                  ┌──────────────────┐
         ▼                                  │ Optimal time     │
┌──────────────────┐                        │ window from      │
│   Separability   │◄───────────────────────│ merged image     │
│   Comparison     │                        │ time series      │
└──────────────────┘                        └────────┬─────────┘
                                                      │
                                                      ▼
┌──────────────────┐      ┌──────────────────┐
│    Accuracy      │◄─────│ SVM classification│◄────
│   assessment     │      └──────────────────┘
└──────────────────┘
```

### 3.2. Extension of the Jeffries–Matusita Distance

In this study, we used the JM distance to measure the period-by-period separability for each pair of crops, because previous research has shown that JM distance can provide a more accurate classification than other distance measures, such as Euclidean distance or divergence [10,19]. The JM distance between a pair of class-specific functions is given by:

$$JM(c_i, c_j) = \int_x \left( \sqrt{p(x|c_i)} - \sqrt{p(x|c_j)} \right)^2 dx \tag{2}$$

where $x$ denotes a span of VI time series values and $c_i$ and $c_j$ (lowercase c) denote the two crop classes under consideration. Under normality assumptions, Equation (2) is reduced to $JM = 2(1 - e^{-B})$, where:

$$B = \frac{1}{8}(\mu_i - \mu_j)^T \left( \frac{C_i + C_j}{2} \right)^{-1} (\mu_i - \mu_j) + \frac{1}{2}\ln\left( \left| \frac{|C_i + C_j|}{2\sqrt{|C_i| \times |C_j|}} \right| \right) \tag{3}$$

and $C_i$ and $C_j$ (uppercase C) are the covariance matrixes of class $i$ and $j$, respectively. Additionally, $|C_i|$ and $|C_j|$ are the determinants of $C_i$ and $C_j$, respectively. The JM distance ranges from 0 to 2, with a large value indicating a high level of separability between two classes [20].

When considering the separability of multi-classes, the weights of different classes are different, because sample amounts for different classes vary. To select optimal temporal windows for multi-class cases, an extension of the JM distance, $J_{Bh}$, was used. The $J_{Bh}$ distance is based on Bhattacharyya bounds; and it is calculated by Equation (4). It gives greater importance to classes with high *a priori* probabilities in the selection process [21].

$$J_{Bh} = \sum_{i=1}^{N} \sum_{j>i}^{N} \sqrt{p(w_i) \times p(w_j) \times JM^2(i,j)} \tag{4}$$

where "*N*" is the number of classes, $p(w_i)$ and $p(w_j)$ are the *a priori* probabilities of class *i* and *j*, which were calculated using the combination of training and validation samples in Table 3.

### 3.3. Optimal Time Period Selection

To understand how separability changes over the growing season, we examined the JM distance of training samples during the entire growing season and every time period for all pair-wise crops. When selecting the optimal temporal window, we first selected the single time period with the highest $J_{Bh}$ distance. Then, we combined any one of the other time periods to the selected period, calculated the $J_{Bh}$ distances of all possible combinations and selected the combination of the largest $J_{Bh}$ distances as the optimal time period combination. Finally, we repeated the process to obtain the optimal combination order.

### 3.4. Support Vector Machine (*SVM*)

SVM is a commonly used classifier whose performance appears to be well suited for remote sensing applications [22]. SVMs use kernel functions to transform nonlinear correlations into a higher (Euclidean or Hilbert) space, making the problem linearly separable and allowing the detection of the hyperplane with the maximum margin. Then, one-against-one and one-against-others methods are applied to solve multi-class problems. The classification result, probabilistic output and certainty of single classifiers were obtained through the integration of single classifiers. To implement the training and modeling procedure, we used the SVM library (libSVM) [23]. The regression model used in this research was the epsilon SVR with a radial basis function (RBF) as the kernel type. In addition, the training of the SVM includes choosing a kernel parameter $\gamma$ and a regularization parameter C (cost). C controls the penalty associated with misclassified training samples, and $\gamma$ determines the gamma of the kernel function. In this study, C and $\gamma$ were selected using a genetic algorithm [24]. Multi-spectral bands and NDVI time series of training samples (Table 3) were used to train the SVM model, and crop labels of the validation samples were predicted with the SVM model. Then, the results were confirmed using the crop labels of the validation samples.

In this research, a confusion matrix and overall accuracy (OA) were employed to evaluate the performance of the entire time series and optimal temporal windows. OA is computed as dividing the number of correctly classified pixels (*i.e.*, the sum of the major diagonal of the matrix) by the total number of pixels in the confusion matrix. This is one of the simplest descriptive statistics derived from a confusion matrix to assess the accuracy of the SVM classification results [25].

## 4. Results and Discussion

### 4.1. Similarity Evaluation for Landsat-5 TM and HJ-1 CCD Data

Three matching images (acquired in May, July and September) were used to compare the similarity between Landsat-5 TM and HJ-1 CCD data in both study areas. The scatter plots and linear relationships of multi-spectral bands and NDVI for the matching images are shown in Figures 4 and 5 for Bole and Manas, respectively. In both study areas, the $R^2$ values are larger than 0.9 for both multi-spectral bands and NDVI, which coincides with previous research and indicates that Landsat-5 TM and HJ-1 CCD data have a strong linear relationship [26–29]. The slopes for the first three bands (Bands 1, 2 and 3) are slightly larger than one, which indicates that Landsat-5 TM data are more sensitive to radiometric changes in these bands. For the fourth band, the slope is less than one, suggesting that HJ-1 CCD data are more sensitive to changes in Band 4. Overall, HJ-1 CCD and Landsat-5 TM images have a similar spatial resolution, spectral bands and radiometric performance. Therefore, multi-spectral bands and NDVI data from both sensors were utilized to obtain the time series for this research.

### 4.2. Separability of Different Crops and Optimal Time Period Selection

We merged Landsat-5 TM and HJ-1 CCD images to obtain time series at 30-m spatial and 15-day temporal resolutions, which contain both multi-spectral bands and NDVI. Then, JM distances were used to analyze the separability of crops within each time period and throughout the entire growing season. JM distances for each pair-wise crop for the entire growing season (Table 4) were higher than 1.95, which shows that crops have a high level of separability in both study areas.

Period-by-period JM distances in Bole and Manas (Figures 6 and 7) show that wheat is highly separable (JM > 1.9) from summer crops throughout the entire year. Wheat and wheat-maize have high levels of separability in July (JM > 1.9), because wheat is harvested and summer maize has developed during that time period. Among summer crops, the greatest separability occurs during the "initial spring green-up phase" and/or "late senescence phase" [30]. For example, a high degree of separability between watermelon and the other summer crops (JM > 1.5) occurs mainly in September, because the growing season for watermelon is shorter than that for the other summer crops. Cotton and maize also have their highest separability in September, which reflects the earlier senescence of maize. Similarly, grape is most discernible from cotton during the April–May and August–September periods, which again reflects different rates of growing and senescence.

**Figure 4.** Scatter plots of the land surface reflectance and NDVI data from HJ-1 CCD and Landsat-5 TM images of Bole.
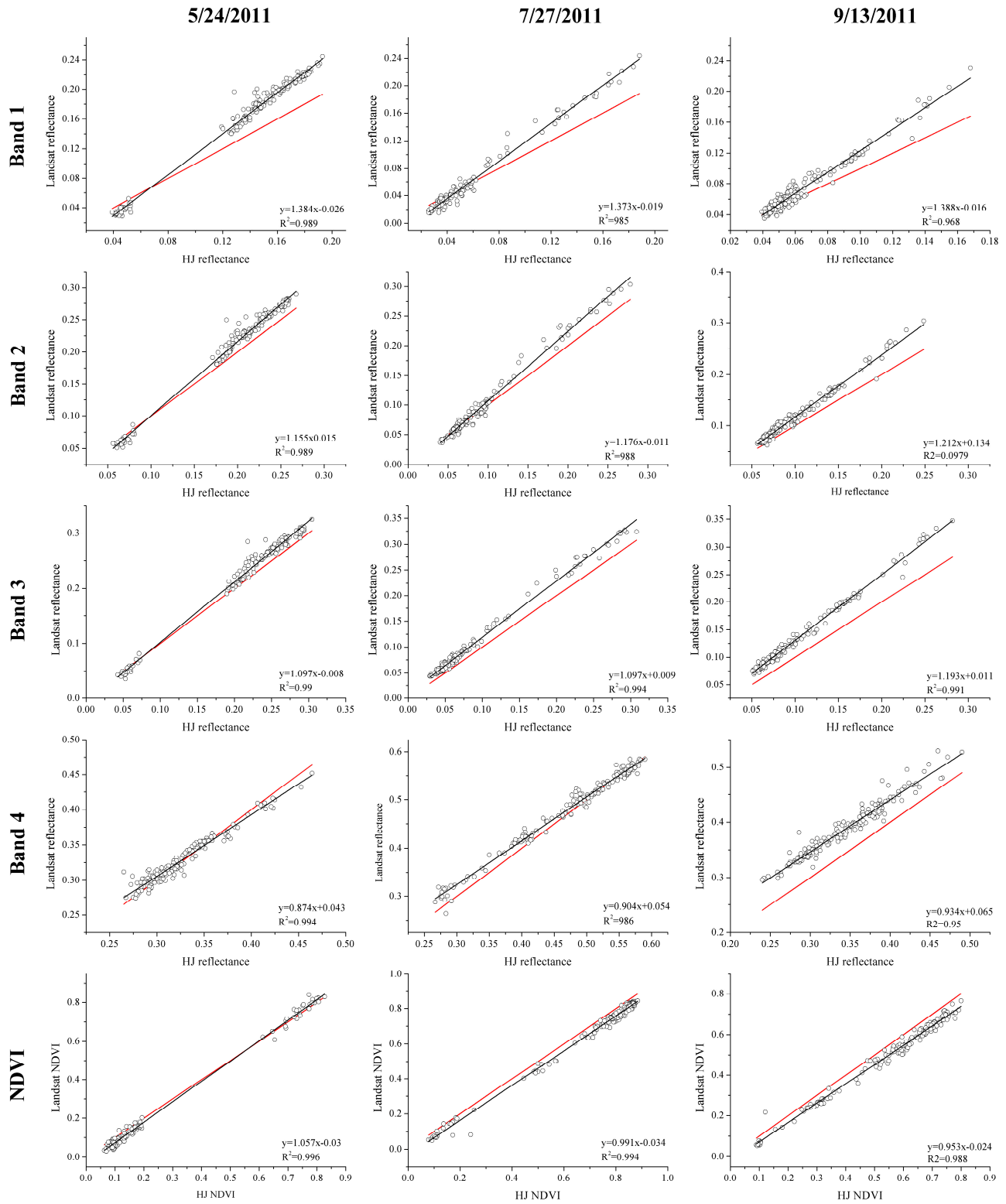


Notes: The red line is 1:1 line.

**Figure 5.** Scatter plots of land surface reflectance and NDVI data from HJ-1 CCD and Landsat-5 TM images of Manas.
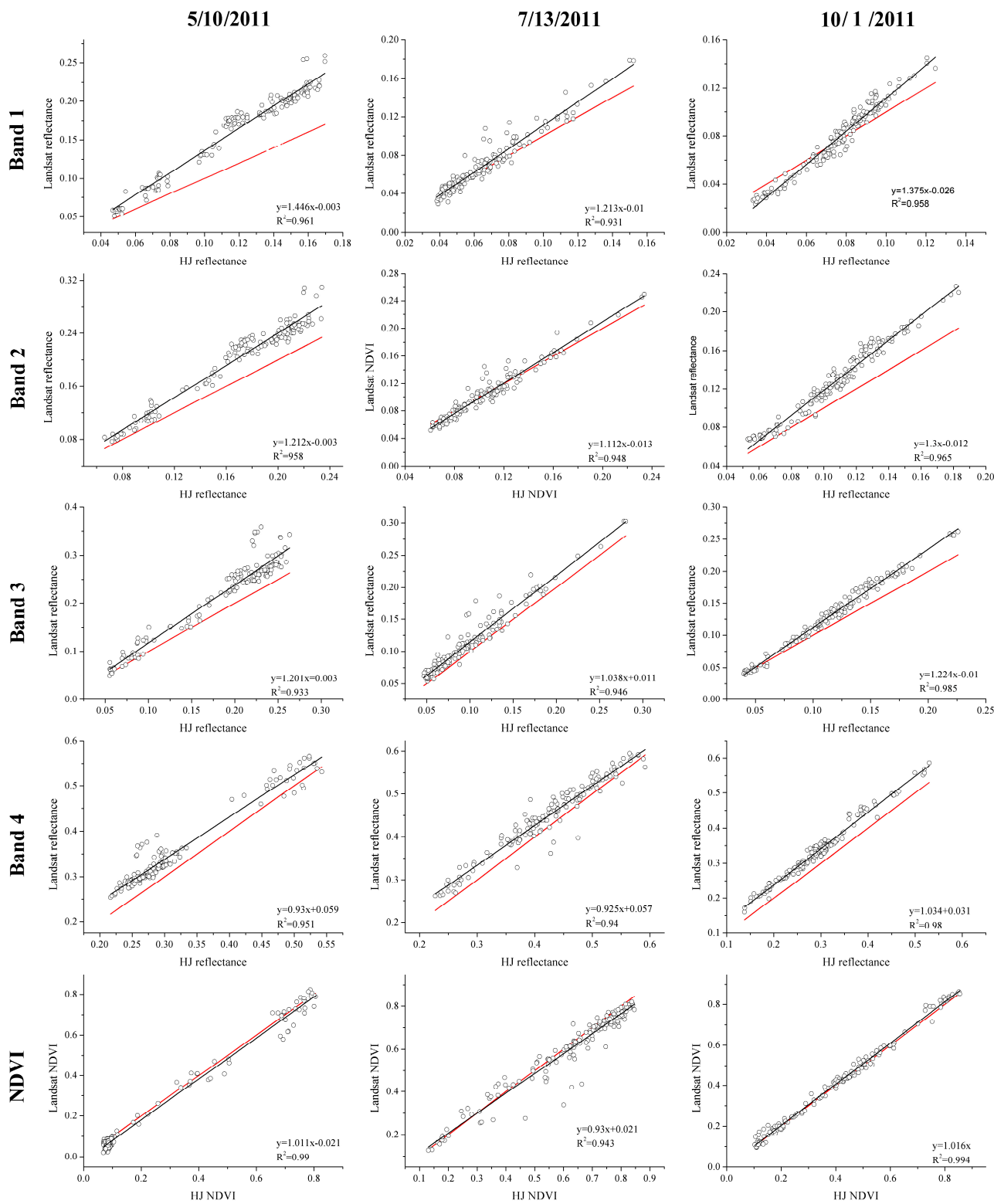


Notes: The red line is 1:1 line.

**Figure 6.** JM distance values for all pair-wise crop comparisons for the entire time series using training samples from Bole.
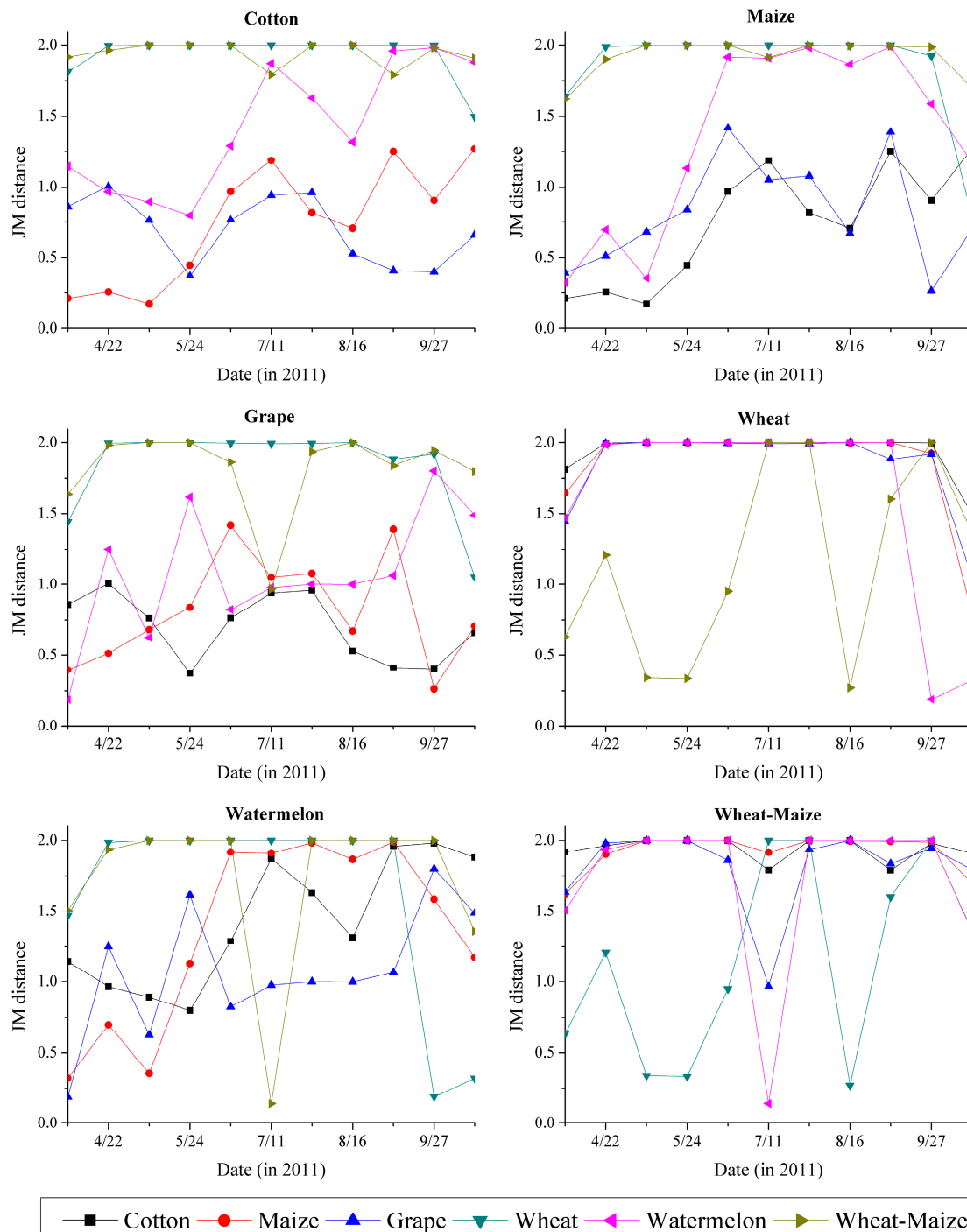


Table 5 shows the order of scene combinations for Bole and Manas using merged time series. We selected four scene combinations for Bole and two scene combinations for Manas (in bold) as optimal temporal windows for crop classification (Table 6), because adding other images increased the separability by only a small degree (*i.e.*, $J_{Bh}$ increased by less than 0.2). Because Bole and Manas have different crops (Figures 6 and 7), the selected optimal temporal windows are different in the two study regions.

**Figure 7.** JM distances values for all pair-wise crop comparisons for the entire time series using training samples from Manas.



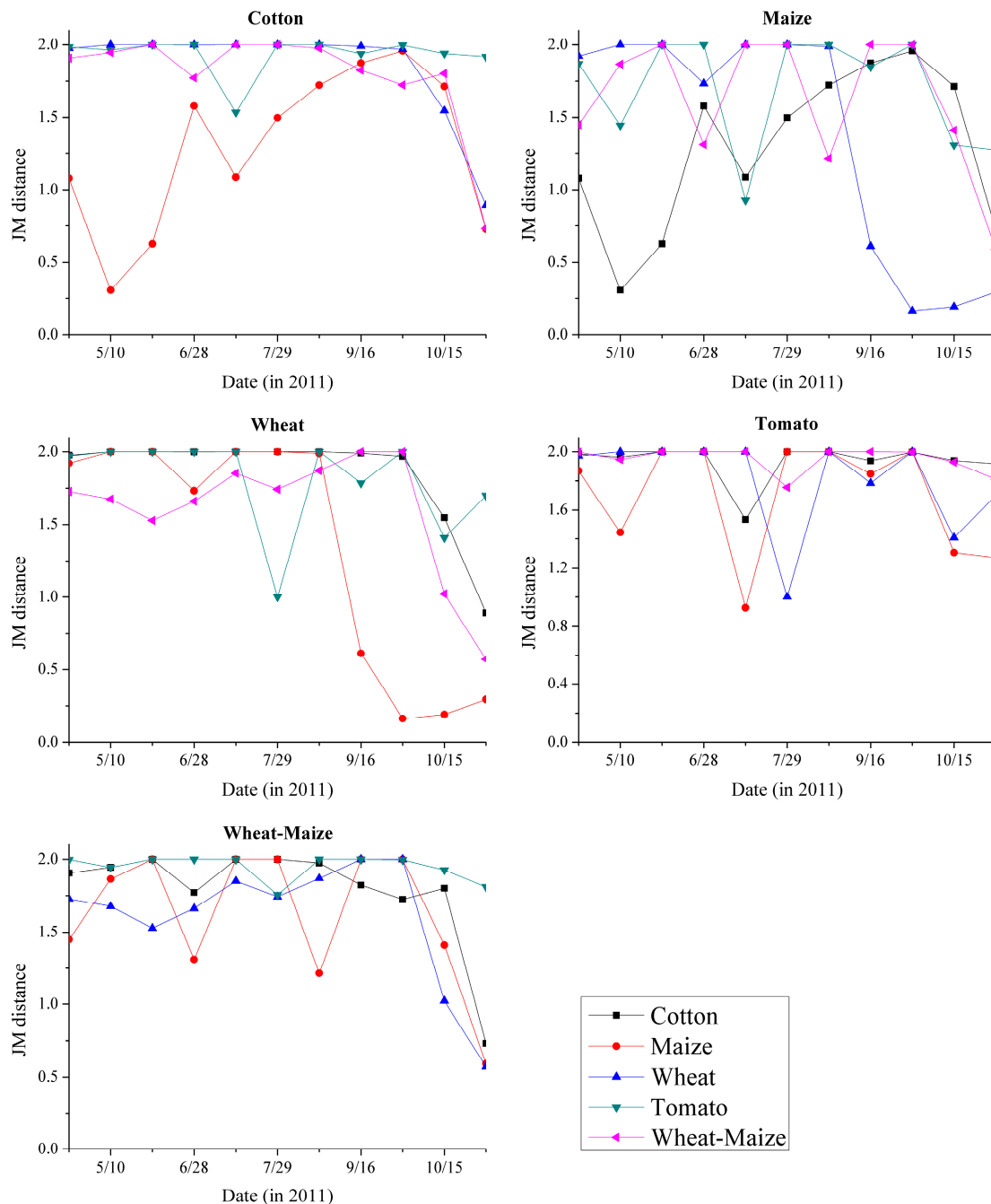In Bole, the optimal temporal periods are mainly in April, September and October, whereas in Manas, the selected temporal periods are mainly in July and September. For a comparison, the same number of TM image combinations (in bold) were also selected. In Manas, all optimal images are TM images, whereas in Bole, the separable level of optimal time periods selected from merged data is slightly higher than that of optimal periods selected from TM time series only ($J_{Bh}$ is 0.2 greater) (Table 7). This is because the merged data cover the optimal temporal window better than TM data alone. For example, in Bole, Landsat-5 TM did not record a cloud-free image in October. Generally, although it is possible to obtain all images at optimal time periods using a single sensor, merged time series have a higher temporal resolution and are more likely to comprise images in the optimal temporal windows.

**Table 4.** Jeffries–Matusita (JM) distances for all pair-wise crop comparisons for the entire time series.

| Crop Type | Maize | Grape | Wheat | Watermelon | Wheat-Maize |
|---|---|---|---|---|---|
| Overall separability of entire growing season in Bole | | | | | |
| Cotton | 1.975 | 1.961 | 2 | 2 | 2 |
| Maize | | 2 | 2 | 2 | 2 |
| Grape | | | 2 | 2 | 2 |
| Wheat | | | | 2 | 2 |
| Watermelon | | | | | 2 |

| Crop Type | Maize | Wheat | Tomato | Wheat-Maize |
|---|---|---|---|---|
| Overall separability of entire growing season in Manas | | | | |
| Cotton | 2 | 2 | 2 | 2 |
| Maize | | 2 | 2 | 2 |
| Wheat | | | 2 | 2 |
| Tomato | | | | 2 |

**Table 5.** Scene combination and their extension of JM distances for the entire time series.

| Scene Combination Number | Bole | | Mans | |
|---|---|---|---|---|
| | Extension JM Distance | Scene Combination | Extension JM Distance | Scene Combination |
| 11 | 9.554 | 1 2 3 4 5 6 7 8 9 10 11 | 7.584 | 1 2 3 4 5 6 7 8 9 10 11 |
| 10 | 9.547 | 1 2 3 4 5 6 8 9 10 11 | 7.584 | 1 2 4 5 6 7 8 9 10 11 |
| 9 | 9.537 | 1 2 3 4 5 6 8 9 11 | 7.584 | 1 2 4 5 6 7 8 9 10 |
| 8 | 9.525 | 1 2 3 5 6 8 9 11 | 7.584 | 1 2 4 5 6 7 8 9 |
| 7 | 9.499 | 1 2 3 5 8 9 11 | 7.584 | 1 4 5 6 7 8 9 |
| 6 | 9.424 | 1 2 3 8 9 11 | 7.584 | 1 4 5 6 7 9 |
| 5 | 9.307 | 1 2 8 9 11 | 7.584 | 1 5 6 7 9 |
| **4** | **9.151** | **1 2 9 11** | 7.583 | 1 5 6 9 |
| **3** | **8.930** | **2 9 11** | 7.581 | 1 6 9 |
| **2** | **8.596** | **2 9** | **7.554** | **6 9** |
| **1** | **7.074** | **9** | **6.860** | **6** |

**Table 6.** JM distance for all pairwise crop comparisons for the optimal temporal window.

| Crop Type | Maize | Grape | Wheat | Watermelon | Wheat-Maize |
|---|---|---|---|---|---|
| Selected time periods in Bole: TM (7/27 and 9/13) HJ1A-CCD1 (6/8) and HJ1A-CCD2 (10/16) | | | | | |
| Cotton | 1.742 | 1.526 | 2 | 2 | 2 |
| Maize | | 1.984 | 2 | 2 | 2 |
| Grape | | | 2 | 1.98 | 2 |
| Wheat | | | | 2 | 2 |
| Watermelon | | | | | 2 |

| Crop Type | Maize | Wheat | Tomato | Wheat-Maize |
|---|---|---|---|---|
| Selected time periods in Manas: TM (7/13, 7/29), HJ1B-CCD1 (9/16) and HJ1A-CCD2 (10/15) | | | | |
| Cotton | 1.997 | 2 | 2 | 2 |
| Maize | | 2 | 2 | 2 |
| Wheat | | | 2 | 2 |
| Tomato | | | | 2 |

**Table 7.** Scenes combination and their extension of JM distances for the TM time series.

| Scene Combination Number | Bole | | Mans | |
| --- | --- | --- | --- | --- |
| | Extension JM Distance | Scene Combination | Extension JM Distance | Scene Combination |
| 6 | 9.186 | 1 2 4 6 7 9 | 7.428 | 1 2 4 5 6 9 |
| 5 | 9.017 | 1 2 6 7 9 | 7.428 | 1 3 4 5 6 |
| **4** | **8.898** | **1 2 7 9** | 7.428 | 1 4 5 6 |
| 3 | 8.763 | 1 2 9 | 7,427 | 1 5 6 |
| 2 | 8.596 | 2 9 | **7.424** | **5 6** |
| 1 | **7.074** | **9** | **6.860** | **6** |

Admittedly, single sensors could record time series at high temporal resolution and provide images covering the optimal temporal window sometimes. For example, Van Niel and McVicar [9] obtained 17 scenes of ETM+ images and selected the optimal temporal window from the entire time series. However, their study area, which was completely covered by two overlapping Landsat paths, was extremely small. In large areas, it is difficult to obtain sufficient cloud-free data at a high temporal resolution with a single sensor. Ju and Roy [31] discovered the possibility of acquiring cloud-free images for the years 2001 and 2003, and their results showed that we can acquire at least one cloud-free Landsat ETM+ observation per year for the majority of global land scenes. However, the possibility of acquiring cloud-free images in each season is limited to only about 50% during winter and fall and 60% during summer and spring on average, and it is much more difficult to acquire cloud-free Landsat images for large areas at a 15-day temporal resolution in a large area. A limited number of images acquired from a single sensor can be used for crop classification [32]. For example, Conrad, *et al.* [33] showed that using two images from a single sensor to map dominating crops could produce acceptable accuracy. However, in high-agrodiversity regions, classification results could be further improved by a fusion of Landsat data with remotely sensed data from other sensing systems and selecting the optimal temporal steps [10].

### 4.3. Pixel-Based Classification Accuracy

Classification accuracies and kappa statistics for Bole and Manas were estimated using validation samples (Tables 8 and 9). Bolded numbers represent pixels that are correctly classified. The overall accuracies for both the entire time series and the optimal temporal window are above 90%, and the kappa coefficients are higher than 0.9, which is acceptable for crop mapping.

In the classification results for the Bole optimal temporal window, both producer's accuracies (PA) and user's accuracies (UA) for cotton, watermelon, winter wheat and wheat-maize are over 90%. Grape has the lowest UA (72.92%), because 354 cotton pixels were mislabeled as grape, which is consistent with the results from Section 4.2 that cotton and grape have the lowest separability level among all pair-wise crops in the optimal temporal window. For other crops, maize has the lowest PA (80.29%). When the entire time series is used, overall accuracy improves (96.49%) and the number of correctly classified pixels of all crop types increases. In particular, nearly all maize pixels are labeled correctly, but more than 200 cotton pixels are still mislabeled.

**Table 8.** Evaluation of crop classification performance in the Bole study area for the entire time series and optimal temporal window using the SVM classifier.

| Classified Data | Reference Data | | | | | | PA (%) |
|---|---|---|---|---|---|---|---|
| | Cotton | Grape | Maize | Watermelon | Wheat | Wheat-Maize | |
| Classification using the optimal temporal window where kappa = 0.9017 and overall accuracy = 93.05% | | | | | | | |
| Cotton | **4155** | 354 | 16 | 17 | 0 | 0 | 91.48% |
| Grape | 24 | **1085** | 0 | 34 | 0 | 0 | 94.93% |
| Maize | 65 | 22 | **383** | 7 | 0 | 0 | 80.29% |
| Watermelon | 0 | 13 | 1 | **1025** | 5 | 0 | 98.18% |
| Wheat | 0 | 0 | 0 | 14 | **1024** | 0 | 98.65% |
| Wheat-Maize | 41 | 14 | 0 | 3 | 1 | **781** | 92.98% |
| UA (%) | 96.97% | 72.92% | 95.75% | 93.18% | 99.42% | 100.00% | |
| Classification using the entire time series where kappa = 0.9500 and overall accuracy = 96.49% | | | | | | | |
| Cotton | **4323** | 215 | 4 | 0 | 0 | 0 | 95.18% |
| Grape | 50 | **1089** | 0 | 4 | 0 | 0 | 95.28% |
| Maize | 10 | 4 | **463** | 0 | 0 | 0 | 97.06% |
| Watermelon | 1 | 3 | 0 | **1040** | 0 | 0 | 99.62% |
| Wheat | 0 | 2 | 0 | 12 | **1024** | 0 | 98.65% |
| Wheat-Maize | 14 | 0 | 0 | 0 | 0 | **826** | 98.33% |
| UA (%) | 98.29% | 82.94% | 99.14% | 98.48% | 100.00% | 100.00% | |

**Table 9.** Evaluation of crop classification performance in the Manas study area for the entire time series and optimal temporal window using the SVM classifier.

| Classified Data | Reference Data | | | | | UA (%) |
|---|---|---|---|---|---|---|
| | Cotton | Maize | Tomato | Wheat | Wheat-Maize | |
| Classification using the optimal temporal window where kappa = 0.9163 with overall accuracy as 94.18% | | | | | | |
| Cotton | **3929** | 57 | 79 | 2 | 14 | 96.28% |
| Maize | 8 | **1619** | 47 | 0 | 0 | 96.71% |
| Tomato | 6 | 44 | **774** | 9 | 0 | 92.92% |
| Wheat | 2 | 55 | 169 | **1241** | 1 | 84.54% |
| Wheat-Maize | 0 | 0 | 0 | 1 | **433** | 99.77% |
| PA (%) | 99.59% | 91.21% | 72.40% | 99.04% | 96.65% | |
| Classification using the entire time series where kappa = 0.9182 with overall accuracy as 94.32% | | | | | | |
| Cotton | **3935** | 56 | 73 | 5 | 12 | 96.42% |
| Maize | 9 | **1613** | 52 | 0 | 0 | 96.36% |
| Tomato | 4 | 46 | **774** | 9 | 0 | 92.92% |
| Wheat | 3 | 26 | 185 | **1253** | 1 | 85.35% |
| Wheat-Maize | 0 | 0 | 0 | 1 | **433** | 99.77% |
| PA (%) | 99.60% | 92.65% | 71.40% | 98.82% | 97.09% | |

In Manas, both the optimal temporal window and entire time series achieve similar classification accuracy, with overall accuracies above 90%. Cotton, maize and wheat-maize are easily distinguished from the other crops, with PA and UA above 90%. Wheat is difficult to separate from tomato, because more than 150 wheat samples were mislabeled as tomato, and tomato was also confused with other crops (cotton and maize).

When comparing data for the entire time series and optimal temporal window, the former exhibits only slightly higher classification accuracy. This indicates that using optimal time periods leads to acceptable classification accuracy (for example, overall accuracy better than 90%), and adding more images has little positive effect on improving classification accuracy. Other studies have also observed this phenomenon when using multi-temporal, multi-spatial and microwave data for classifying crop types [9–11,34,35]. However, accurate crop classification depends on "optimal scene selection," and misclassification may occur due to a lack of data in the "optimal temporal window" [10].

### 4.4. Scene Combination Order Using Different Sample Sizes

We varied training sample sizes from 10% to 90% of the entire training samples and extracted the scene combination order using different sample amounts. Five repetitions were randomly selected for each sample size (Table 10). The bolded scenes are the selected temporal periods. In both study areas, when the training sample size is 80% or 90% of the entire sample size, the scene combination order varies little, and the selected temporal periods are equal to those using all training samples. Conversely, when the number of training samples is between 30% and 60% of the entire sample size, the scene combination order changes slightly and, in most cases, the majority of the selected optimal temporal periods is equal to those selected using the entire sample size. For example, when the training sample size is 40% of the entire sample size, three out of four selected time periods are the same as the optimal temporal periods for both Bole and Manas (Table 5). However, when the training sample size is less than 20%, the scene combinations for the five repetitions vary significantly, and the selected time periods are different from the optimal time windows (Table 5), especially in Bole. This may be because the training sample size is too small (about 300 training samples), and the change of selected time periods is attributed to some atypical samples. Overall, the same optimal temporal windows will be identified when training samples are sufficiently large (more than 30% of the entire training sample size).

**Table 10.** Scenes combination order with different sample sizes.

| Sample Size | Scene Combination Order in Bole | | | | | | | | | | | Scene Combination Order in Manas | | | | | | | | | | |
|---|---|---|---|---|---|---|---|---|---|---|---|---|---|---|---|---|---|---|---|---|---|---|
| 90% | **9** | **2** | **11** | **1** | 8 | 3 | 5 | 6 | 4 | 10 | 7 | **6** | **9** | 1 | 5 | 7 | 4 | 8 | 2 | 10 | 11 | 3 |
| | **9** | **2** | **11** | **1** | 8 | 3 | 5 | 6 | 7 | 4 | 10 | **6** | **9** | 5 | 7 | 1 | 4 | 8 | 2 | 10 | 11 | 3 |
| | **9** | **2** | **11** | **1** | 8 | 3 | 5 | 6 | 4 | 10 | 7 | **6** | **9** | 1 | 4 | 7 | 5 | 8 | 10 | 2 | 11 | 3 |
| | **9** | **2** | **11** | **1** | 8 | 3 | 5 | 6 | 4 | 7 | 10 | **6** | **9** | 1 | 5 | 7 | 4 | 8 | 2 | 10 | 11 | 3 |
| | **9** | **2** | **11** | **1** | 8 | 3 | 5 | 6 | 4 | 10 | 7 | **6** | **9** | 1 | 4 | 7 | 5 | 8 | 10 | 3 | 11 | 2 |
| 80% | **9** | **2** | **11** | **1** | 8 | 3 | 5 | 6 | 4 | 10 | 7 | **6** | **9** | 1 | 4 | 7 | 5 | 8 | 10 | 3 | 11 | 2 |
| | **9** | **2** | **11** | **1** | 8 | 3 | 5 | 6 | 4 | 10 | 7 | **6** | **9** | 1 | 4 | 7 | 5 | 8 | 2 | 10 | 11 | 3 |
| | **9** | **2** | **11** | **1** | 8 | 3 | 5 | 6 | 7 | 4 | 10 | **6** | **9** | 1 | 4 | 7 | 5 | 8 | 10 | 3 | 11 | 2 |
| | **9** | **2** | **11** | **1** | 8 | 3 | 5 | 6 | 10 | 4 | 7 | **6** | **9** | 1 | 5 | 7 | 4 | 8 | 11 | 10 | 2 | 3 |
| | **9** | **2** | **7** | **1** | 3 | 8 | 5 | 11 | 6 | 10 | 4 | **6** | **9** | 1 | 4 | 7 | 5 | 8 | 10 | 2 | 11 | 3 |
| 70% | **9** | **2** | **11** | **1** | 8 | 3 | 5 | 6 | 4 | 7 | 10 | **6** | **9** | 1 | 5 | 7 | 4 | 8 | 10 | 2 | 11 | 3 |
| | **9** | **2** | **8** | **1** | 3 | 5 | 6 | 11 | 7 | 10 | 4 | **6** | **9** | 5 | 1 | 7 | 4 | 8 | 2 | 10 | 11 | 3 |
| | **7** | **10** | **2** | **3** | 1 | 8 | 5 | 11 | 6 | 9 | 4 | **6** | **9** | 1 | 5 | 7 | 4 | 11 | 10 | 8 | 2 | 3 |
| | **9** | **2** | **11** | **1** | 8 | 3 | 5 | 4 | 6 | 10 | 7 | **6** | **9** | 1 | 5 | 7 | 4 | 11 | 10 | 2 | 8 | 3 |
| | **9** | **2** | **7** | **1** | 3 | 8 | 5 | 6 | 11 | 10 | 4 | **6** | **9** | 1 | 4 | 7 | 5 | 8 | 2 | 10 | 11 | 3 |

**Table 10.** *Cont.*

| Sample Size | Scene Combination Order in Bole | | | | | | | | | | | Scene Combination Order in Manas | | | | | | | | | | |
|---|---|---|---|---|---|---|---|---|---|---|---|---|---|---|---|---|---|---|---|---|---|---|
| 60% | 7 | 10 | 1 | 5 | 8 | 3 | 2 | 11 | 6 | 9 | 4 | 6 | 9 | 1 | 5 | 4 | 7 | 8 | 10 | 11 | 3 | 2 |
| | 9 | 2 | 1 | 8 | 3 | 5 | 11 | 6 | 4 | 10 | 7 | 6 | 9 | 5 | 1 | 4 | 7 | 8 | 10 | 3 | 11 | 2 |
| | 9 | 2 | 11 | 1 | 8 | 3 | 5 | 6 | 7 | 10 | 4 | 6 | 9 | 1 | 4 | 7 | 5 | 8 | 10 | 11 | 2 | 3 |
| | 9 | 2 | 8 | 1 | 3 | 5 | 6 | 11 | 4 | 10 | 7 | 6 | 9 | 1 | 4 | 7 | 5 | 8 | 10 | 11 | 2 | 3 |
| | 9 | 2 | 1 | 8 | 3 | 5 | 11 | 6 | 7 | 10 | 4 | 6 | 9 | 1 | 5 | 4 | 7 | 8 | 3 | 10 | 11 | 2 |
| 50% | 9 | 2 | 11 | 1 | 8 | 3 | 5 | 6 | 10 | 4 | 7 | 6 | 9 | 1 | 4 | 7 | 5 | 8 | 10 | 3 | 2 | 11 |
| | 9 | 2 | 10 | 8 | 3 | 1 | 5 | 11 | 6 | 7 | 4 | 6 | 9 | 1 | 4 | 7 | 2 | 8 | 10 | 5 | 3 | 11 |
| | 9 | 2 | 8 | 1 | 3 | 5 | 6 | 11 | 4 | 7 | 10 | 6 | 9 | 5 | 1 | 4 | 7 | 2 | 8 | 10 | 11 | 3 |
| | 9 | 2 | 11 | 3 | 1 | 8 | 5 | 6 | 7 | 10 | 4 | 6 | 9 | 1 | 5 | 4 | 7 | 11 | 10 | 2 | 8 | 3 |
| | 9 | 2 | 11 | 1 | 8 | 3 | 5 | 6 | 4 | 10 | 7 | 6 | 9 | 1 | 7 | 5 | 4 | 8 | 11 | 10 | 2 | 3 |
| 40% | 9 | 2 | 1 | 8 | 3 | 5 | 11 | 6 | 10 | 7 | 4 | 6 | 9 | 1 | 4 | 7 | 8 | 2 | 10 | 11 | 5 | 3 |
| | 9 | 2 | 8 | 1 | 5 | 11 | 3 | 6 | 7 | 4 | 10 | 6 | 9 | 1 | 5 | 7 | 8 | 4 | 10 | 2 | 11 | 3 |
| | 9 | 2 | 11 | 3 | 8 | 1 | 5 | 10 | 4 | 6 | 7 | 6 | 9 | 1 | 5 | 7 | 4 | 8 | 2 | 10 | 3 | 11 |
| | 7 | 10 | 1 | 8 | 5 | 3 | 2 | 11 | 4 | 6 | 9 | 6 | 8 | 1 | 9 | 7 | 5 | 4 | 3 | 10 | 2 | 11 |
| | 9 | 2 | 8 | 3 | 10 | 5 | 1 | 11 | 6 | 7 | 4 | 6 | 9 | 1 | 4 | 7 | 10 | 5 | 8 | 11 | 3 | 2 |
| 30% | 7 | 10 | 8 | 1 | 3 | 4 | 5 | 9 | 2 | 11 | 6 | 6 | 9 | 5 | 1 | 4 | 7 | 8 | 11 | 10 | 2 | 3 |
| | 9 | 2 | 1 | 8 | 3 | 5 | 11 | 6 | 7 | 4 | 10 | 6 | 9 | 5 | 4 | 1 | 7 | 8 | 10 | 2 | 11 | 3 |
| | 9 | 2 | 11 | 1 | 8 | 3 | 5 | 10 | 6 | 7 | 4 | 6 | 9 | 1 | 5 | 4 | 7 | 8 | 2 | 10 | 3 | 11 |
| | 9 | 2 | 11 | 1 | 8 | 3 | 5 | 4 | 6 | 7 | 10 | 6 | 8 | 1 | 7 | 5 | 9 | 4 | 2 | 10 | 3 | 11 |
| | 9 | 2 | 1 | 6 | 3 | 8 | 5 | 11 | 4 | 10 | 7 | 6 | 9 | 1 | 5 | 4 | 2 | 7 | 8 | 10 | 3 | 11 |
| 20% | 9 | 2 | 1 | 8 | 3 | 11 | 6 | 7 | 4 | 5 | 10 | 5 | 9 | 1 | 7 | 8 | 6 | 11 | 2 | 3 | 4 | 10 |
| | 9 | 2 | 3 | 10 | 1 | 7 | 5 | 6 | 11 | 4 | 8 | 6 | 9 | 1 | 4 | 7 | 8 | 10 | 2 | 5 | 3 | 11 |
| | 9 | 2 | 1 | 8 | 3 | 5 | 6 | 7 | 11 | 4 | 10 | 6 | 9 | 4 | 5 | 1 | 7 | 8 | 10 | 11 | 2 | 3 |
| | 7 | 10 | 8 | 1 | 3 | 2 | 5 | 9 | 4 | 11 | 6 | 6 | 8 | 1 | 7 | 5 | 9 | 4 | 10 | 11 | 3 | 2 |
| | 7 | 10 | 1 | 8 | 3 | 2 | 11 | 4 | 6 | 5 | 9 | 6 | 9 | 10 | 11 | 1 | 4 | 7 | 2 | 8 | 3 | 5 |
| 10% | 7 | 2 | 8 | 1 | 9 | 3 | 4 | 6 | 5 | 10 | 11 | 6 | 9 | 1 | 11 | 2 | 3 | 4 | 5 | 7 | 8 | 10 |
| | 8 | 5 | 1 | 3 | 10 | 6 | 11 | 4 | 9 | 2 | 7 | 6 | 9 | 1 | 5 | 3 | 4 | 7 | 2 | 8 | 10 | 11 |
| | 7 | 2 | 10 | 8 | 1 | 5 | 3 | 4 | 6 | 9 | 11 | 6 | 9 | 4 | 7 | 3 | 5 | 1 | 2 | 8 | 10 | 11 |
| | 9 | 2 | 1 | 11 | 6 | 8 | 3 | 4 | 7 | 5 | 10 | 5 | 8 | 7 | 4 | 2 | 1 | 3 | 6 | 9 | 10 | 11 |
| | 9 | 11 | 7 | 1 | 5 | 3 | 2 | 6 | 4 | 8 | 10 | 6 | 9 | 1 | 4 | 2 | 3 | 5 | 7 | 8 | 10 | 11 |

## 5. Conclusions

In this study, we evaluated the radiometric similarity between Landsat-5 TM and HJ-1 CCD data and estimated the potential of time series merged from two sensors for crop classification in the Chinese counties of Bole and Manas. Our main conclusions are as follows.

(1) Landsat-5 TM and HJ-1 CCD images have similar NDVI and radiometric performances in multi-spectral bands. Therefore, missing Landsat-5 TM data can be replaced by HJ-1 CCD data, and we were able to obtain time series at 30-m spatial and high temporal resolution by merging Landsat-5 TM and HJ-1 CCD data.

(2) In agreement with previous research, time series in optimal temporal windows can achieve high classification accuracies, and additional images did not significantly increase separability and overall accuracy. Moreover, data, classes and samples influence the selected temporal periods.

As for data, the merged time series have a higher temporal resolution and a higher likelihood of containing images in the optimal temporal windows. Therefore, optimal temporal periods selected from merged time series have slightly higher separable levels than those selected from single-sensor time series. In addition, different crop types affect the optimal temporal windows because the optimal temporal periods used for differentiating between different crops varied. Normally, the same optimal time periods will be selected when using different training samples. However, if the training sample size is too small (*i.e.*, less than 300), untypical samples will lead to variances of the scene combination order.

Using merged time series for accurate crop classification is especially promising for large regions, because multi-sensors increase the possibility of acquiring time series at medium spatial resolution (about 30 m) with high temporal resolution. Additionally, accurate crop distribution maps can contribute to determining regional water requirements for irrigation [36,37]. As more data at medium spatial resolution, such as Gaofen (GF-1) with a 16-m spatial resolution [15], become available, we will continue to study merged data from additional sensors.

## Acknowledgments

## Author Contributions

Pentyu Hao, Li Wang and Zheng Niu designed the research, Li Wang and Abdullah Aablikim collected the field data. Pengyu Hao processed the Landsat and HJ data for crop classification and wrote the paper. Ni Huang, Shiguang Xu and Fang Chen contributed important ideas and considerations.

## Conflicts of Interest

The authors declare no conflict of interest.

## References

1. Pan, Y.Z.; Li, L.; Zhang, J.S.; Liang, S.L.; Zhu, X.F.; Sulla-Menashe, D. Winter wheat area estimation from MODIS-EVI time series data using the crop proportion phenology index. *Remote Sens. Environ.* **2012**, *119*, 232–242.
2. Guerschman, J.P.; Paruelo, J.M.; di Bella, C.; Giallorenzi, M.C.; Pacin, F. Land cover classification in the argentine pampas using multi-temporal Landsat TM data. *Int. J. Remote Sens.* **2003**, *24*, 3381–3402.
3. Claverie, M.; Demarez, V.; Duchemin, B.; Hagolle, O.; Ducrot, D.; Marais-Sicre, C.; Dejoux, J.F.; Huc, M.; Keravec, P.; Beziat, P.; *et al.* Maize and sunflower biomass estimation in southwest France using high spatial and temporal resolution remote sensing data. *Remote Sens. Environ.* **2012**, *124*, 844–857.

4. Benhadj, I.; Duchemin, B.; Maisongrande, P.; Simonneaux, V.; Khabba, S.; Chehbouni, A. Automatic unmixing of modis multi-temporal data for inter-annual monitoring of land use at a regional scale (Tensift, Morocco). *Int. J. Remote Sens.* **2012**, *33*, 1325–1348.

5. Pan, Y.Z.; Hu, T.G.; Zhu, X.F.; Zhang, J.S.; Wang, X.D. Mapping cropland distributions using a hard and soft classification model. *IEEE Trans. Geosci. Remote Sens.* **2012**, *50*, 4301–4312.

6. Lhermitte, S.; Verbesselt, J.; Verstraeten, W.W.; Coppin, P. A comparison of time series similarity measures for classification and change detection of ecosystem dynamics. *Remote Sens. Environ.* **2011**, *115*, 3129–3152.

7. Pena-Barragan, J.M.; Ngugi, M.K.; Plant, R.E.; Six, J. Object-based crop identification using multiple vegetation indices, textural features and crop phenology. *Remote Sens. Environ.* **2011**, *115*, 1301–1316.

8. Vieira, M.A.; Formaggio, A.R.; Renno, C.D.; Atzberger, C.; Aguiar, D.A.; Mello, M.P. Object based image analysis and data mining applied to a remotely sensed Landsat time-series to map sugarcane over large areas. *Remote Sens. Environ.* **2012**, *123*, 553–562.

9. Van Niel, T.G.; McVicar, T.R. Determining temporal windows for crop discrimination with remote sensing: A case study in south-eastern Australia. *Comput. Electron. Agric.* **2004**, *45*, 91–108.

10. Murakami, T.; Ogawa, S.; Ishitsuka, N.; Kumagai, K.; Saito, G. Crop discrimination with multitemporal SPOT/HRV data in the Saga Plains, Japan. *Int. J. Remote Sens.* **2001**, *22*, 1335–1348.

11. Jia, K.; Wu, B.; Li, Q. Crop classification using HJ satellite multispectral data in the North China plain. *J. Appl. Remote Sens.* **2013**, *7*, doi:10.1117/1.JRS.7.073576.

12. Zhu, S.; Zhou, W.; Zhang, J.S.; Shuai, G.Y. Wheat acreage detection by extended support vector analysis with multi-temporal remote sensing images. In Proceedings of the 2012 First International Conference on Agro-Geoinformatics (Agro-Geoinformatics), Shanghai, China, 2–4 August 2012; pp. 603–606.

13. Jiang, B.; Liang, S.; Townshend, J.R.; Dodson, Z.M. Assessment of the radiometric performance of Chinese HJ-1 satellite CCD instruments. *IEEE J. Sel. Top. Appl. Earth Obs. Remote Sens.* **2013**, *6*, 840–850.

14. Carrao, H.; Goncalves, P.; Caetano, M. Contribution of multispectral and multiternporal information from MODIS images to land cover classification. *Remote Sens. Environ.* **2008**, *112*, 986–997.

15. China Center for Resource Satellite Data and Application. Available online: http://www.cresda.com/n16/n1115/n1522/n2118/index.html (accessed on 25 July 2014).

16. Landsat 5 History. Available online: http://landsat.usgs.gov/about_landsat5.php (accessed on 25 July 2014).

17. Chander, G.; Markham, B.L.; Helder, D.L. Summary of current radiometric calibration coefficients for Landsat MSS, TM, ETM+, and EO-1 ALI sensors. *Remote Sens. Environ.* **2009**, *113*, 893–903.

18. Vanonckelen, S.; Lhermitte, S.; van Rompaey, A. The effect of atmospheric and topographic correction methods on land cover classification accuracy. *Int. J. Appl. Earth Obs. Geoinf.* **2013**, *24*, 9–21.

19. Van Niel, T.G.; McVicar, T.R.; Datt, B. On the relationship between training sample size and data dimensionality: Monte Carlo analysis of broadband multi-temporal classification. *Remote Sens. Environ.* **2005**, *98*, 468–480.

20. Adam, E.; Mutanga, O. Spectral discrimination of papyrus vegetation (*Cyperus Papyrus* L.) in swamp wetlands using field spectrometry. *ISPRS J. Photogramm. Remote Sens.* **2009**, *64*, 612–620.

21. Bruzzone, L.; Roli, F.; Serpico, S.B. An extension of the Jeffreys-Matusita distance to multiclass cases for feature selection. *IEEE Trans. Geosci. Remote Sens.* **1995**, *33*, 1318–1321.

22. Mountrakis, G.; Im, J.; Ogole, C. Support vector machines in remote sensing: A review. *ISPRS J. Photogramm. Remote Sens.* **2011**, *66*, 247–259.

23. Chang, C.C.; Lin, C.J. LIBSVM: A library for support vector machines. *ACM Trans. Intell. Syst. Technol.* **2011**, *2*, 27.

24. Low, F.; Michel, U.; Dech, S.; Conrad, C. Impact of feature selection on the accuracy and spatial uncertainty of per-field crop classification using support vector machines. *ISPRS J. Photogramm. Remote Sens.* **2013**, *85*, 102–119.

25. Congalton, R.G. A review of assessing the accuracy of classifications of remotely sensed data. *Remote Sens. Environ.* **1991**, *37*, 35–46.

26. Huang, N.; He, J.S.; Niu, Z. Estimating the spatial pattern of soil respiration in Tibetan alpine grasslands using Landsat TM images and MODIS data. *Ecol. Indic.* **2013**, *26*, 117–125.

27. Huang, W.J.; Huang, J.F.; Wang, X.Z.; Wang, F.M.; Shi, J.J. Comparability of red/near-infrared reflectance and NDVI based on the spectral response function between MODIS and 30 other satellite sensors using rice canopy spectra. *Sensors* **2013**, *13*, 16023–16050.

28. Agapiou, A.; Alexakis, D.D.; Hadjimitsis, D.G. Spectral sensitivity of ALOS, ASTER, IKONOS, Landsat and SPOT satellite imagery intended for the detection of archaeological crop marks. *Int. J. Digit. Earth* **2014**, *7*, 351–372.

29. Tong, A.; He, Y.H. Comparative analysis of SPOT, Landsat, MODIS, and AVHRR normalized difference vegetation index data on the estimation of leaf area index in a mixed grassland ecosystem. *J. Appl. Remote Sens.* **2013**, *7*, doi:10.1117/1.JRS.7.073599.

30. Wardlow, B.D.; Egbert, S.L.; Kastens, J.H. Analysis of time-series MODIS 250 m vegetation index data for crop classification in the U.S. Central Great Plains. *Remote Sens. Environ.* **2007**, *108*, 290–310.

31. Ju, J.C.; Roy, D.P. The availability of cloud-free Landsat ETM plus data over the conterminous united states and globally. *Remote Sens. Environ.* **2008**, *112*, 1196–1211.

32. Marshall, G.J.; Dowdeswell, J.A.; Rees, W.G. The spatial and temporal effect of cloud cover on the acquisition of high quality Landsat imagery in the European arctic sector. *Remote Sens. Environ.* **1994**, *50*, 149–160.

33. Conrad, C.; Fritsch, S.; Zeidler, J.; Rücker, G.; Dech, S. Per-field irrigated crop classification in arid central Asia using SPOT and ASTER data. *Remote Sens.* **2010**, *2*, 1035–1056.

34. Shao, Y.; Fan, X.; Liu, H.; Xiao, J.; Ross, S.; Brisco, B.; Brown, R.; Staples, G. Rice monitoring and production estimation using multitemporal Radarsat. *Remote Sens. Environ.* **2001**, *76*, 310–325.

35. Zhou, F.Q.; Zhang, A.N.; Townley-Smith, L. A data mining approach for evaluation of optimal time-series of MODIS data for land cover mapping at a regional level. *ISPRS J. Photogramm. Remote Sens.* **2013**, *84*, 114–129.

36. Conrad, C.; Rahmann, M.; Machwitz, M.; Stulina, G.; Paeth, H.; Dech, S. Satellite based calculation of spatially distributed crop water requirements for cotton and wheat cultivation in Fergana Valley, Uzbekistan. *Glob. Planet. Chang.* **2013**, *110*, 88–98.

37. Zhong, L.H.; Gong, P.; Biging, G.S. Phenology-based crop classification algorithm and its implications on agricultural water use assessments in California's Central Valley. *Photogramm. Eng. Remote Sens.* **2012**, *78*, 799–813.